

MJO change with A1B global warming estimated by the 40-km ECHAM5

Ping Liu · Tim Li · Bin Wang · Minghua Zhang · Jing-jia Luo ·
Yukio Masumoto · Xiaocong Wang · Erich Roeckner

Received: 7 May 2012 / Accepted: 10 September 2012
© Springer-Verlag 2012

Abstract This study estimates MJO change under the A1B greenhouse gas emission scenario using the ECHAM5 AGCM whose coupled version (ECHAM5/MPI-OM) has simulated best MJO variance among fourteen CGCMs. The model has a horizontal resolution at T319 (about 40 km) and is forced by the monthly evolving SST derived from the ECHAM5/MPI-OM at a lower resolution of T63 (about 200 km). Two runs are carried out covering the last 21 years of the twentieth and twenty-first centuries. The NCEP/NCAR Reanalysis products and observed precipitation are used to validate the simulated MJO during the twentieth century, based on which the twenty-first century MJO change is compared and predicted. The validation

indicates that the previously reported MJO variances in the T63 coupled version are reproduced by the 40-km ECHAM5. More aspects of MJO, such as the eastward propagation, structure, and dominant frequency and zonal wavenumber in power spectrum, are simulated reasonably well. The magnitude in power, however, is still low so that the signal is marginally detectable and embedded in the over-reddened background. Under the A1B scenario, the T63 ECHAM5/MPI-OM projected an over 3 K warmer tropical sea surface that forces the 40-km ECHAM to produce wetter tropics. The enhanced precipitation variance shows more spectral enhancement in background than in most wavebands. The zonal winds associated with MJO, however, are strengthened in the lower troposphere but weakened in the upper. On the one hand, the 850-hPa zonal wind has power nearly doubled in 30–60-days bands, demonstrating relatively clearer enhancement than the precipitation in MJO with the warming. A 1-tailed Student's *t* test suggests that most of the MJO changes in variance and power spectra are statically significant. Subject to a 20–100-days band-pass filtering of that wind, an EOF analysis indicates that the two leading components in the twentieth-century run have a close structure to but smaller percentage of explained-to-total variance than those in observations; the A1B warming slightly increases the explained percentage and alters the structure. An MJO index formed by the two leading principal components discloses nearly doubling in the number of prominent MJO events with a peak phase occurring in February and March. A composite MJO life cycle of these events favors the frictional moisture convergence mechanism in maintaining the MJO and the nonlinear wind-induced surface heat exchange (WISHE) mechanism also appears in the A1B warming case. On the other hand, the Slingo index based on the 300-hPa zonal wind discloses that the upper-level

P. Liu · T. Li · B. Wang
International Pacific Research Center, SOEST,
University of Hawaii at Manoa, Honolulu, HI, USA

P. Liu (✉) · M. Zhang
School of Marine and Atmospheric Sciences, Stony Brook
University, 199 Endeavour Hall, SoMAS, Stony Brook,
NY 11794-5000, USA
e-mail: Ping.Liu@stonybrook.edu

J. Luo · Y. Masumoto
Research Institution for Global Change, Japan Agency for
Marine-Earth Science and Technology, Kanagawa, Japan

J. Luo
Centre for Australian Weather and Climate Research,
Bureau of Meteorology, Melbourne, Australia

X. Wang
The State Key Laboratory of Numerical Modeling for
Atmospheric Sciences and Geophysical Fluid Dynamics
(LASG), Beijing, China

E. Roeckner
Max Planck Institute for Meteorology, Hamburg, Germany

MJO tends to be suppressed by the A1B warming, although the loose relationship with ENSO remains unchanged. Possible cause for the different change of MJO in the lower and upper troposphere is discussed.

Keywords MJO · A1B scenario · Global warming

1 Introduction

Madden-Julian oscillation (MJO; Madden and Julian 1971, 1972) dominates the tropical troposphere variability on 20–80 days by contributing more than 40 % to the total variance in precipitation and zonal wind anomalies (e.g. Liu et al. 2005). This dominant signal substantially impacts monsoons (Yasunari 1979; Waliser 2006), effectively stimulates ENSO (Zhang 2005), and significantly extends medium-range weather forecast predictability (Waliser et al. 1999). Since the Fourth Assessment Report (AR4) by the Intergovernmental Panel on Climate Change (IPCC; IPCC 2007) projected that global warming will continue in the coming decades even due to the inertia of the climate system with the greenhouse gas emission remaining at current levels, how the MJO will change with the anthropogenic global warming is important for the mitigation and impact estimation of climate change.

Slingo et al. (1999) reported that the MJO was consistently more active during the decade after the mid-1970s than during the one before. They attributed the active trend of the MJO to the rise of sea surface temperature in the tropics and thus anticipated that the MJO would be more active with the anthropogenic global warming. Jones and Carvalho (2006) also noted that a change of MJO regime occurs in the late 1970s with positive trends in anomalies and greater number of MJO events. Like Slingo et al., they related the increasing MJO activity to the warming SST in the tropical Indian and Pacific oceans (Jones and Carvalho 2011a) by using a non-homogeneous stochastic model constructed from observations (Jones and Carvalho 2011b). Their model further projected that the MJO may become more active given the projected SST change under the A1B greenhouse gas emission scenario (Jones and Carvalho 2011a). Nevertheless, the stochastic model can hardly estimate the change in MJO dynamical features such as power spectra, eastward propagation, structure, and associated physical processes. These characteristics can be better estimated by a global climate model.

Dynamical simulation of MJO remains overall unsatisfactory by contemporary coupled and uncoupled global climate models (GCMs; Slingo et al. 1996; Lin et al. 2006). Most GCMs produce the MJO variability too low. Some models simulate an MJO-like signal with too short dominant period and too large phase speed moving eastward.

Others have MJO-like signals with equivalent power in eastward and westward moving components forming a standing structure (Zhang 2005; Lin et al. 2006; Randall et al. 2007). Because of the unsatisfactory simulation, possible changes of the MJO under different IPCC greenhouse gas emission scenarios have not been predicted faithfully so as to document in the IPCC AR4.

The first-order changes of the MJO features and associated processes were estimated by Liu (2012) using an idealized aqua-planet AGCM. With the globally uniform warming of 2 and 4 K in surface temperature, the model predicted the MJO to be more active with overall enhanced tropical precipitation and more prominent MJO events to occur. The MJO power would be enhanced more on shorter time scales with more robust leading EOF structures. A composite life cycle of the prominent MJO events indicated that both the frictional moisture convergence (e.g. Wang 1988; Hendon and Salby 1994; Maloney and Hartmann 1998) and nonlinear wind induced surface heat exchange (WISHE; e.g. Maloney and Sobel 2004) mechanisms became more established to maintain the enhanced MJO activity. In spite of the estimated changes consistent with those obtained by Jones and Carvalho (2011a) using a stochastic model, this aqua-planet GCM produced the MJO power peak at zonal wavenumber 2, a feature not occurring predominantly in historical records, and this was speculated due to the lack of the basic-state Walker circulation. Such deficiencies call for a complete GCM to do the MJO projection that is also consistent with the changing climate.

The MPI-ECHAM5/OM developed at the Max Planck Institute for Meteorology, among the 14 coupled models in comparison, simulated some MJO features arguably the closest to observations (Lin et al. 2006). For example, the precipitation variance of MJO in this model approaches the observed value in both Indian Ocean and Western Pacific where the MJO has peak phases, while the variance in the Indian Ocean in the second best model and everywhere in the rest models is less than half of that observed, just as weak as that in earlier AGCMs (Slingo et al. 1996); the eastward propagation of MJO is also distinctive to its westward counterpart. This model's advantageous performance, despite of some notable deficiencies discussed by Lin et al. (2006), suggests its ability to produce MJO changes more reliably than other GCMs. Using the atmospheric component of this model, this study projects MJO features under one scenario of global warming.

Among the several different emission scenarios, the A1B (Nakicenovic et al. 2000) emphasizes a balance across all energy sources and assumes that similar improvement rates applying to all energy supply and end use technologies, which is probably close to reality. Under the A1B scenario, the AR4 GCMs have projected that the globally averaged surface temperature in 2090–2099 can be 1.7–4.4 °C

warmer (Table SPM.3) with a best estimate of 2.8 °C relative to the 1990–1999 mean. In comparison, the MPI-ECHAM5/OM at horizontal T63 (about 200 km) and vertical 31 layers (T63L31) resolution predicts an average warming of about 3 K in the tropics between 30°S and 30°N while nearly 4 K over the deep tropics (see Fig. 1), a magnitude greater than the average to generate more active MJOs shown below.

The monthly-evolving SST from the T63L31 MPI-ECHAM5/OM is used to force the atmospheric component ECHAM5 at T319 (about 40 km) for two 21-years transient experiments: one for the twentieth century climate (HIS_20C hereafter); the other for the twenty-first climate change under the A1B scenario (A1B_21C hereafter). Several variables at daily interval are archived, which makes it possible to compare the MJO in the HIS_20C with that observed, and furthermore to predict the MJO change in the A1B_21C. Section 2 briefly describes the ECHAM5 model, the SST derived from the MPI-ECHAM5/OM, observational data sets, and the methodology to derive the MJO features. Section 3 compares the simulated MJO characteristics with those observed and analyzes the MJO change in the HIS_20C run. Summary and discussion are given in Sect. 4.

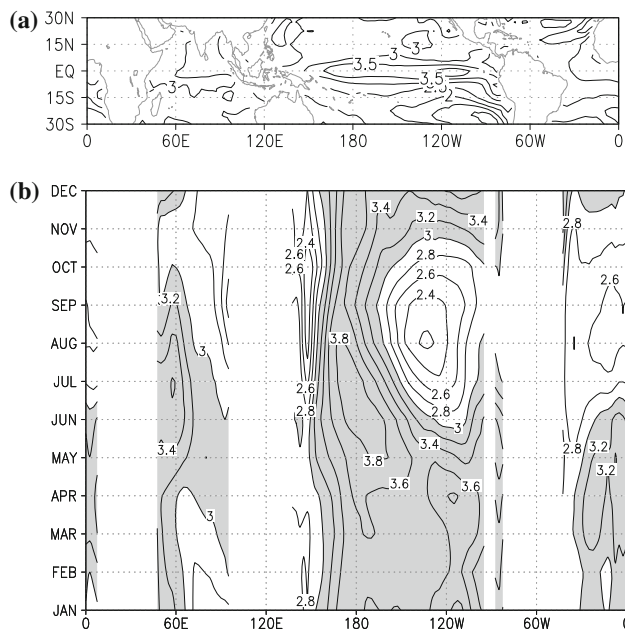


Fig. 1 **a** Change of SST (K) in the tropics during the DJFM season projected by the T63 ECHAM5/MPI-OM under the A1B scenario. Shown is the difference of the last-21-years mean in the twenty-first and twentieth centuries. The average change over the entire tropics is 3.05 K. **b** Change of the seasonal cycle in monthly mean SST (K) along the equator (5°S–5°N mean) by the A1B_21C compared to the HIS_20C. Values greater than and equal to 3 K are shaded in gray

2 Model, data and methodology

2.1 Echam5

The ECHAM5 is the atmospheric component of the ECHAM5/MPI-OM coupled model (Jungclaus et al. 2006) developed at the Max Planck Institute for Meteorology. Among the 14 coupled models intercompared (Lin et al. 2006), the ECHAM5 has a comparatively high resolution with vertically 31 layers and horizontally at triangularly truncated 63 waves, corresponding to a latitude/longitude grid of 1.875° or 192 × 96 grid points. In comparison, most other models have a lower horizontal and vertical resolution (c.f. Table 1 in Lin et al. 2006). It is noteworthy that the ECHAM5 used the convection scheme of Tiedtke (1989) revised by Nordeng (1994) to include convective available potential energy (CAPE) in the closure. Moisture convergence is incorporated as a first guess of the cloud base mass flux so that deep convection is somewhat related to the large-scale convergence. This relation was believed important to produce the reasonable MJO features as described in Lin et al. (2006). Detailed description of this model is given by Roeckner et al. (2006).

Expecting that a higher horizontal resolution can better resolve meso-scale processes, we use the SSTs produced by the T63L31 ECHAM5/MPI-OM in the two periods 1980–2000 and 2080–2100 to force the ECHAM5 at T319L31 (960 × 480 grids and about 40 × 40 km² for each). This higher resolution has simulated better tropical cyclone events (Bengtsson et al. 2007) and is expected to produce reasonable MJO features and probable projections. For the HIS_20C, the coupled model is integrated starting from an ocean and atmospheric state obtained from a 500 years pre-industrial integration with observed and reconstructed pre-industrial concentrations of carbon dioxide, methane and nitrous oxide. The well-mixed greenhouse gases, for example CO₂, CH₄, N₂O, F₁₁, F₁₂ and minor halocarbons, are prescribed as annual global means fitting to ice core data and direct observations. Monthly data of stratospheric and tropospheric ozone concentrations are prescribed as two-dimensional distributions in latitude and height. The space-time distribution of sulphate aerosols is prescribed using the data from an offline simulation (Pham et al. 2005). Both the direct and first indirect effects of sulphate aerosols on cloud albedo are included. This integration produces simulations up to the end of the twentieth century. For the A1B_21C, the SRES A1B scenario (Nakicenovic et al. 2000) is used; and the integration ends at the end of the twenty-first century.

2.2 Data

To compare the simulated MJO in the HIS_20C with observations during 1980–2000, we use the zonal winds

from the NCEP-NCAR Reanalysis project (Kalnay et al. 1996). The Reanalysis products are blended outputs from the forecast model and observations; thus they have been serving as an estimate to reality, particularly over most oceans where observations are sparse. Since the precipitation in the Reanalysis is model produced, we use the satellite-based observation from the Global Precipitation Climatology Project (GPCP; Huffman et al. 1997) as a reference.

2.3 MJO indices

The time series of the HIS_20C, A1B_21C, Reanalysis, and GPCP variables are derived in either daily or pentadal mean. Anomalous winds and precipitation in pentad are calculated then filtered with a 20–100-days band pass filter to isolate the MJO signal. Variance, power spectra, and lag correlation are computed to assess the MJO activities such as dominant wavenumber, periods and propagation direction. Since the A1B_21C shows overall positive changes, a 1-tailed Student's t test is applied to the changed climatology in precipitation, and variance and power spectrum associated with MJO.

We form two indices to disclose the MJO features in more detail. The first index is based on an EOF analysis using the filtered 850-hPa zonal wind averaged in 10°S–10°N. Because the upper-level zonal wind associated with MJO shows less coherent change, unlike for example Wheeler and Hendon (2004), it is not included to define the MJO index. The leading two EOFs usually image the salient structure of MJO. Based upon their lead-lag correlation, the corresponding two principal components (PCs) can be combined linearly to form the first index so as to pick prominent MJO events. Specifically, one formula defines the index time series as $IND(t) = PC1(t) + [PC2(t+2) + PC2(t+3)]/2$, where t denotes time in pentads, because the lead-lag correlation coefficients of the two PCs are largest and statistically significant by 1–3 pentads lead/lag, which is similar for the two model cases (not shown). A selected event then must include three consecutive phases of initiation, peak and decay that are constrained by the index values exceeding ± 1 STD. The composite life cycle of these events can be formed to depict the propagating features of the MJO and associated mechanisms. This method has been employed in diagnosing the MJO structures in observations (e.g. Maloney and Hartmann 1998) and in numerical models (e.g. Maloney and Hartmann 2001; Liu 2012). To describe the interannual variability of MJO, the second index is based on the zonal wind at 300 hPa (the wind at 200 hPa was not archived). The band-pass-filtered wind is zonally averaged in 10°S–10°N; and the variance is derived and subject to a 100-days running mean to form the index. We still call it the Slingo

index (Slingo et al. 1996, 1999) since the difference is small.

3 Result

3.1 Mean-state change

Observational study estimates an average of only 0.2 K increase of SST in the tropics and subtropics during the late twentieth century compared to the late nineteenth century (Rayner et al. 2006). However under the A1B greenhouse gas emission scenario, the IPCC AR4 (Table SPM.3) projected substantial SST warming in the late twenty-first century. Specifically for the ECHAM5/MPI-OM, Fig. 1a compares the SST in the A1B_21C with the HIS_20C during the extended boreal winter season (December to March; DJFM hereafter). Clearly the entire tropical ocean surface is over 3 K warmer, reaching the higher end of the IPCC AR4 estimates. The warming is nearly uniform in the Indian Ocean and subtropical North Pacific, similar to the uniform warming specified by Liu (2012) in the aqua-planet experiment. Over the key El Niño regions, the warming is notably above 3.5 K. The warmer SST tends to evaporate more moisture into the atmosphere to induce more convections (Bengtsson et al. 2007), and thus MJO can be more active.

The MJO in observation is more active and has larger amplitudes during boreal spring than other seasons (e.g. Zhang 2005). This seasonality can be modulated by the SST seasonal cycle, particularly under the global warming background. Figure 1b illustrates the projected change in the seasonal cycle of SST averaged in 5°S–5°N, where the MJO is usually most active (e.g. Wang and Rui 1990). During the DJFM season, the A1B_21C SST is 3.2–3.6 K warmer than the HIS_20C; and the warming is nearly zonally uniform, close to what was imposed on an aqua-plane model by Liu (2012), so that similar MJO response can be expected. The SST is more zonally asymmetric in other seasons. For example in May–August, the maximum warming occurs at about 15° from the date line, while from June to October, the weak warming of 2.2 K occurs in the Eastern Pacific.

Corresponding to the warming pattern shown in Fig. 1, most tropical areas become wetter in the DJFM season, as illustrated by the climatological precipitation difference in Fig. 2. Specifically, over 2 mm day^{−1} more precipitation falls to the south of the equator from South America to the Indian Ocean, and over 5 mm day^{−1} more to the tropical Pacific. A notable double ITCZ forms to east of the date line near 10°N and 10°S, which is associated with the SST warming pattern (c.f. Fig. 1a). Most precipitation changes (shading) in the deep tropics are statistically significant at 95 % with the Student's t test.

Fig. 2 Same as Fig. 1a but for the precipitation rate. Contour interval is 1 mm day^{-1} and values above 95 % significance level of a 1-tailed Student t test are shaded in gray

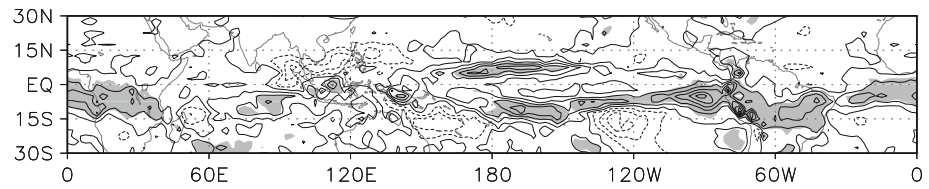
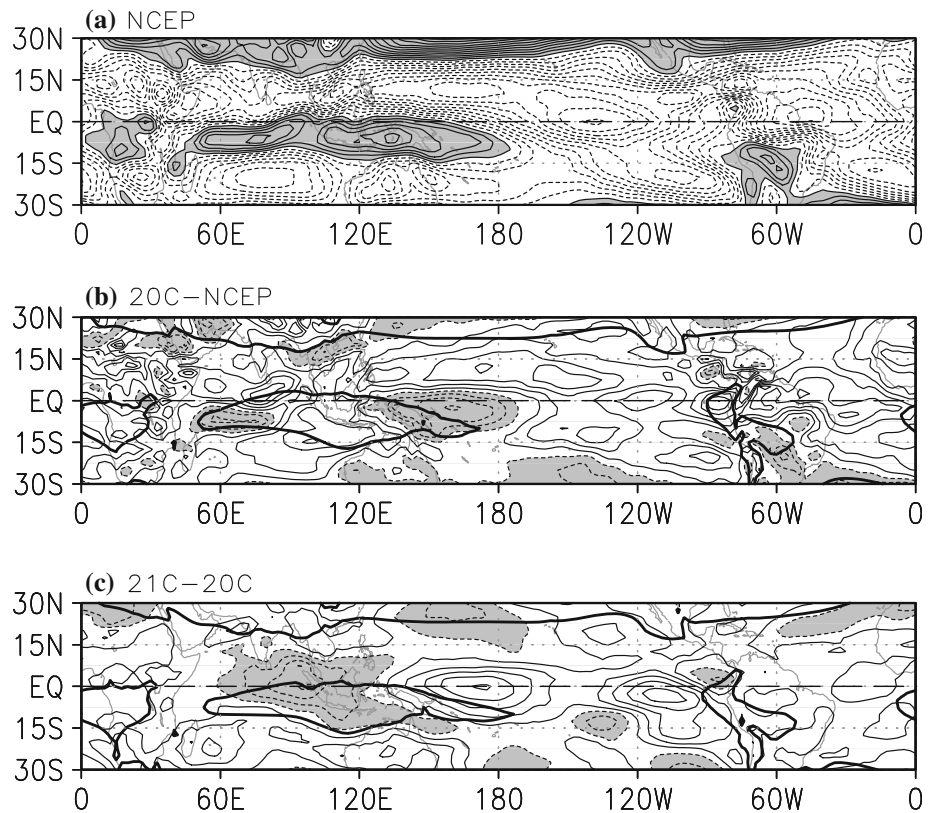


Fig. 3 850-hPa zonal wind in the DJFM season averaged in the last 21 years for **a** NCEP 1981–2000, **b** A1B_20C–NCEP and **c** A1B_21C–HIS_20C. Contour interval is 1 m s^{-1} in (a) and (b), and 0.5 m s^{-1} in (c). Values ≥ 0 in (a), ≤ -1 in (b) and ≤ -0.5 in (c) are shaded. The thick black lines are for 0 in the HIS_20C (b) and the A1B_21C (c)



Background low-level westerly winds are important to maintain the MJO eastward propagation (e.g. Slingo et al. 1996; Inness et al. 2003). In the NCEP–NCAR Reanalysis (Fig. 3a), the 850-hPa westerly winds in DJFM occur in 15°S – 0°N from Africa to the date line and are notably stronger than 5 m s^{-1} near 90°E and 130°E . The HIS_20C (Fig. 3b) has simulated the westerly wind pattern reasonably well in longitudinal range, as circled by the thick solid line, especially in tropical Africa, Indian–West Pacific, and central south America. This westerly pattern corresponds to the reasonable MJO structures in low-level zonal wind to be shown. However, some biases remain. For example, the magnitude is about 3 m s^{-1} weaker in the western Indian Ocean and western Pacific warm pool; the eastern edge is about 10° west of the date line; and it is much stronger over the eastern Indian Ocean to the Maritime Continent. The biases may be responsible for the discrepancies in the simulated MJO.

The A1B_21C warmer tropical surface brings considerable changes in low-level westerly wind, as shown in

Fig. 3c. Although the westerly wind (the black thick circle) has a pattern close to that in the Reanalysis, it becomes weaker in the Indian Ocean—the Maritime Continent with 2 m s^{-1} weaker near 100°E , but stronger in the western Pacific Warm Pool with 2 m s^{-1} stronger near 170°E , forming a dipole pattern. These two locations correspond to the maximum MJO variance in observation (e.g. Hendon and Salby 1994); therefore, the MJO signals can be changed differently in the Indian Ocean and in the western Pacific by the A1B_21C warming. It is noteworthy that this change in the zonal wind is consistent with the weakening of the Walker circulation in a warmer climate (Zhang and Song 2006; Vecchi and Soden 2007), owing to the change of the vertical stability of the tropical atmosphere.

3.2 MJO variance, power spectra and propagation

Lin et al. (2006) reported that the MJO-like signal produced by the fourteen coupled climate models was embedded in the over reddened background. The warmer SST of

A1B_21C makes the tropics wetter (c.f. Fig. 2) so that the background variance in precipitation can be larger. Here we follow the procedure of Wheeler and Kiladis (1999) to derive the power spectra of the background precipitation in the HIS_20C and A1B_21C cases. In Fig. 4a the background power of the HIS_20C is clearly red. Specifically large values are located on periods longer than 30 days and at zonal wave numbers smaller than 5, with a center on periods longer than 60 days and at eastward zonal wave number 1. This distribution agrees with that the MJO is embedded in the over reddened background. The warmer sea surface of A1B_21C makes the background power spectra of precipitation even redder (Fig. 4b). The center is about 0.95 standardized values, more than double of that in the HIS_20C. This center is also located at the zonal wavenumbers 1–3 in eastward direction, indicating the red background for the MJO band is enhanced even more.

To show the overall changes in MJO activity induced by the A1B_21C warming, we calculate the variance

difference in the filtered precipitation and 850-hPa zonal wind from the HIS_20C. The variance difference in precipitation (Fig. 5a) is positive in the entire tropical oceans, suggesting more activity in the MJO band. It is largest in the Indian Ocean and Pacific, in agreement with the climatological precipitation pattern (c.f. Fig. 2). The variance difference increases notably along the double ITCZ, which is likely associated with the enhanced convectively coupled equatorial waves. Most changes (shaded) in the variance are also above 95 % significance level of the t test.

In contrast to the overall enhancement of the precipitation variance, the change of 850-hPa zonal wind variability has fluctuating patterns (Fig. 5b) associated with the change in the mean state (c.f. Fig. 3c). The variance is enhanced in the tropical Western Hemisphere from the eastern Pacific to the western Indian Ocean. While in the 60°E–180°E near the equator where the MJO usually dominates, the variance is either enhanced or weakened. Specifically, it is strengthened notably in north of Australia

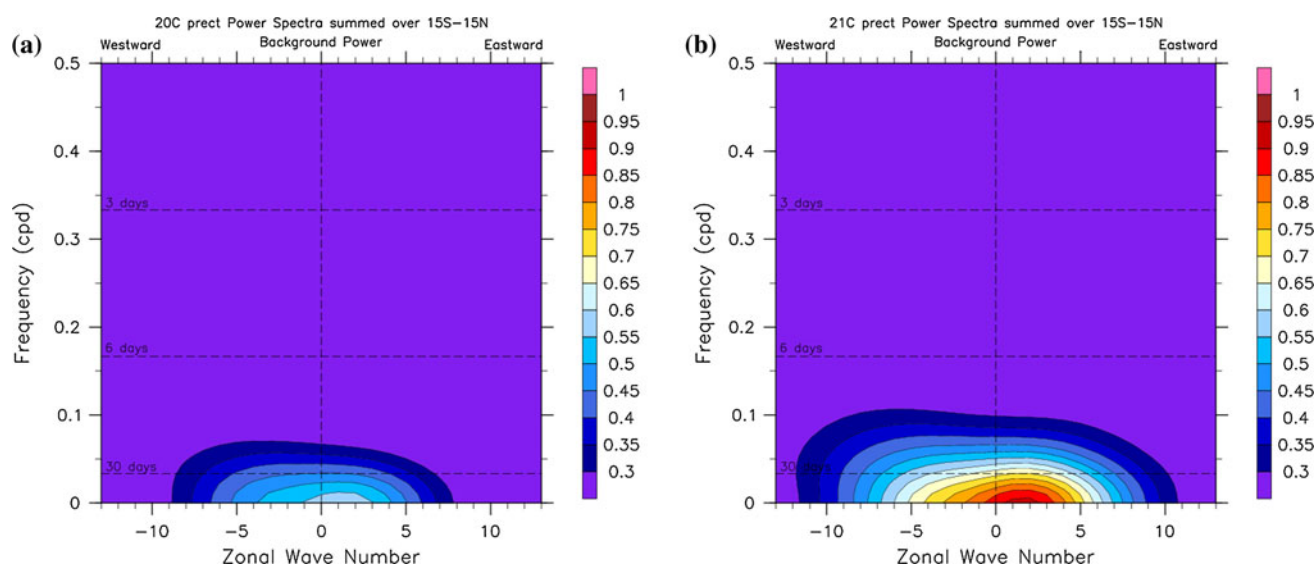
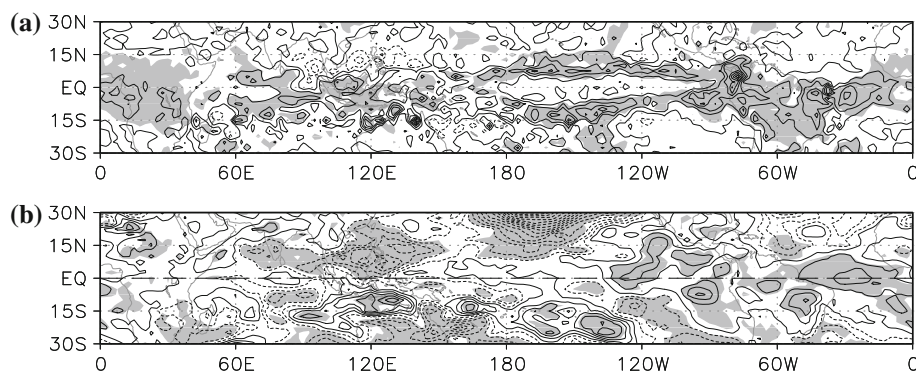


Fig. 4 **a** Background power spectra of precipitation in the HIS_20C derived by the Wheeler and Kiladis (1999) package. **b** Same as Fig. 4a but for the A1B_21C

Fig. 5 **a** Same as Fig. 2 but for the difference of 20–100-days variance of precipitation rate. Contour interval is $10 \text{ mm}^2 \text{ day}^{-2}$ and values above 95 % significance level of the t test are shaded. **b** Same as Fig. 5a but for the 850-hPa zonal wind and shaded are above 90 % significance level of the t test for both positive and negative sides. Contour interval is $0.5 \text{ m}^2 \text{ s}^{-2}$



and near the date line to the South Pacific convergence zone (SPCZ) and slightly enhanced in the central Indian Ocean; it is reduced in most equatorial Indian Ocean, Indonesia and the western Pacific. Interestingly, most changes, either weakening or strengthening, have passed a 90 % significance level of the t test. The changes in 850-hPa zonal wind in the A1B_21C are clearly not consistent with those in precipitation, and more incoherent change will be seen in MJO power spectra and structures.

The dominant periods and zonal wave number, and eastward propagation of MJO usually correspond to a maximum in the wavenumber-frequency power spectrum of precipitation and 850-hPa zonal wind. Figure 6 gives the power spectra for precipitation in the HIS_20C (Fig. 6a) and the difference made by the A1B_21C (Fig. 6b). The HIS_20C power is less than $0.03 \text{ mm}^2 \text{ day}^{-2}$, overall lower than those in observations, for example as documented by Liu et al. (2005) where the central value can be $0.08 \text{ mm}^2 \text{ day}^{-2}$. The relatively large center is near 100 days and at wavenumber between 3 and 4; the value is a little more than 0.025. At low wavenumbers 1–2 and on periods 40–60 days where the MJO usually resides (e.g.

Zhang 2005), the power spectra do not show a clear dominant pattern. Also the power spectra for the westward propagation are small but comparable to the eastward counterparts. Such a power spectral pattern suggests that the precipitation in the HIS_20C does not have a strong eastward propagation in the MJO bands. In the A1B_21C (Fig. 6b), the power spectra are enhanced in nearly all wavenumbers and in both eastward and westward propagation directions, indicating that the enhanced MJO is embedded in the background spectra (c.f. Fig. 4b). It is noteworthy that there is a 0.015 enhancement at zonal wavenumber one and near 45 days; the enhanced value can be 100 % compared to the HIS_20C and passes the 95 % significance level of the t test. Since the MJO power is overall weak, this enhancement can cautiously indicate that the eastward propagating MJO is enhanced in precipitation.

The 850-hPa zonal wind in the HIS_20C has a power spectral pattern similar to the precipitation but with different changes in A1B_21C, as shown in Fig. 7. In the HIS_20C the wind spectra are also weak with a central value about $0.02 \text{ m}^2 \text{ s}^{-2}$ that is much smaller than the $0.08 \text{ m}^2 \text{ s}^{-2}$ in observations (e.g. Liu et al. 2005). However, the eastward propagating component has relatively larger spectra than the westward component in the MJO bands

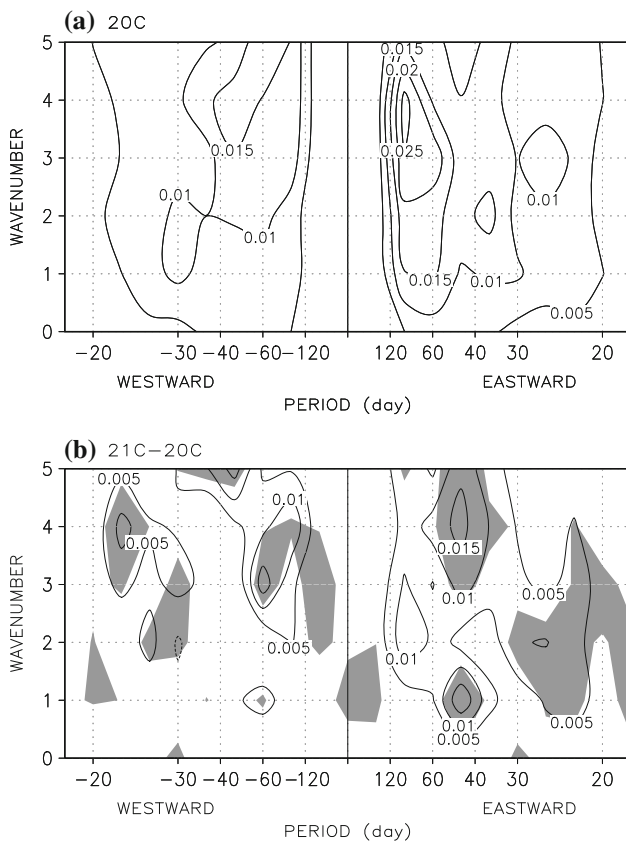


Fig. 6 Wavenumber-frequency power spectra ($\text{mm}^2 \text{ day}^{-2}$) for precipitation averaged in the 20 DJFM seasons over 10°S – 10°N after the 20–100-days band-pass filtering for **a** the HIS_20C and **b** the A1B_21C-HIS_20C. Shaded are above 95 % significance level

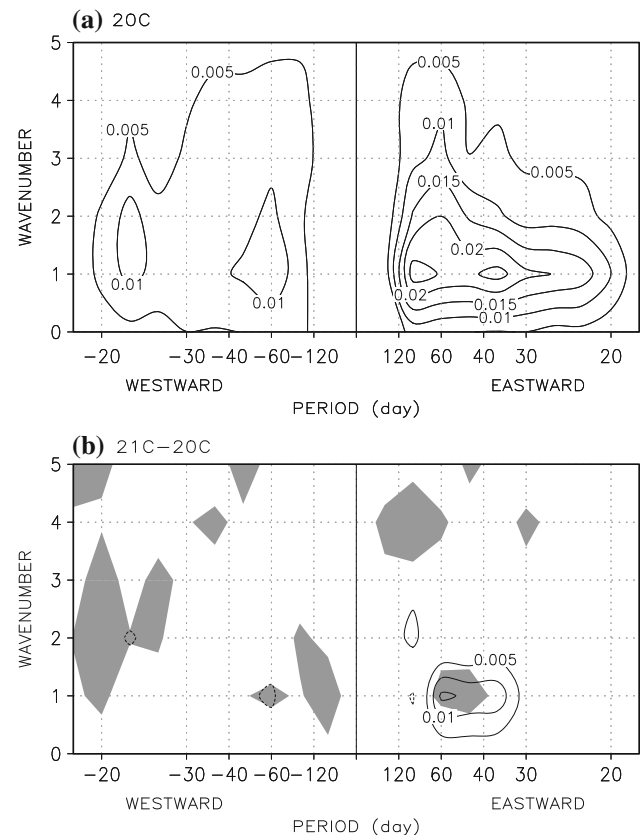


Fig. 7 Same as Fig. 6 but for the 850-hPa zonal wind ($\text{m}^2 \text{ s}^{-2}$). Shaded are above 90 % significance level

and the center is concentrated at zonal wavenumber 1 and on 40 and 100 days. Such a pattern shows some footprints of the MJO that is also embedded in the over reddened background. The A1B_21C has clearly enhanced the power spectra of 850-hPa zonal wind (Fig. 7b). Specifically the power is nearly doubled on 30–60 days and at zonal wavenumber 1 in eastward propagation component, while it changes rarely in other bands. This change has a t test value somewhat lower than the 95 % but higher than the 90 % significance level. It is noteworthy that the power spectra of zonal wind at 300 hPa are weak but tend to be standing; and in the A1B_21C the power spectra are reduced by 30 % (not shown). The reduction in the upper troposphere indicates that the enhancement of the power in 850-hPa zonal wind may be caused by the enhanced shallow convection. We will discuss more about this point in the final section.

A lead-lag correlation map can show the MJO propagation direction and its possible change with the A1B warming, given the weak power spectra in the simulated precipitation and 850-hPa zonal wind. Because the precipitation variance is enhanced nearly in the entire tropics, we select the point at (90°E, 0°N) as the reference against which the lead-lag correlation coefficients are calculated using the 10°S–10°N average daily mean after 20–100-days band-pass filtering. The results are shown in Fig. 8. During the HIS_20C period (Fig. 8a), the eastward propagation of a signal (e.g. the shading contours) starts near 28°E and on the –30th day. It strengthens to about 0.5 at 50°E and on the –15th day then drops to near zero at 65°E and on the –10th day. It then gradually increases to 1 at 90°E and on day 0. The coefficient becomes smaller and drops to about 0.1 at 180°E and on the 30th day. The structure spans nearly 60 days in the eastward propagation, a typical period for the MJO. This map indicates that the ECHAM5 has produced the eastward propagation although the power spectra are low (c.f. Fig. 6a). Notable westward propagation is also seen in the Indian Ocean. For the HIS_21C case, the shading area is broken in the tropical western Indian Ocean, suggesting that the moving MJO is weakened there. In the Eastern Indian ocean to near the date line, the correlation coefficient reaches 0.4, about twice of that in the HIS_20C, indicating that the MJO is somewhat enhanced. The enhancement in the Pacific and suppression in the Indian Ocean of MJO agree well with the weakened Walker circulation described earlier.

The lead-lag correlation maps for the 850-hPa zonal wind show more complete structures in the HIS_20C and A1B_21C cases (Fig. 9). Because the eastward propagation precipitation is more prominent in the eastern Indian Ocean—western Pacific (c.f. Fig. 8), we select the point at 150°E as the reference to construct the lead-lag correlation

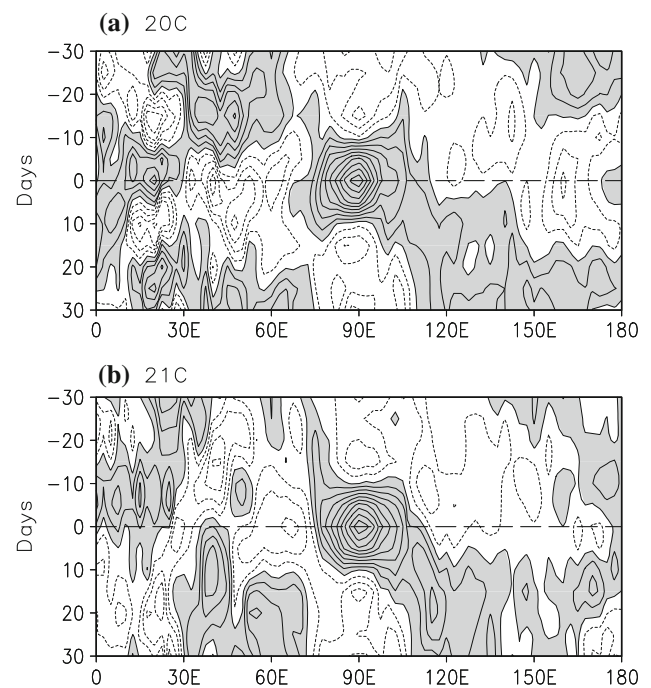


Fig. 8 Lag correlation of 20–100-days filtered precipitation rate averaged in the 20 DJFM seasons for **a** the HIS_20C and **b** the A1B_21C, respectively. The reference point is at (90°E, 0°N) averaged in 10°S–10°N. Contour interval is 0.1 and values ≥ 0 are shaded

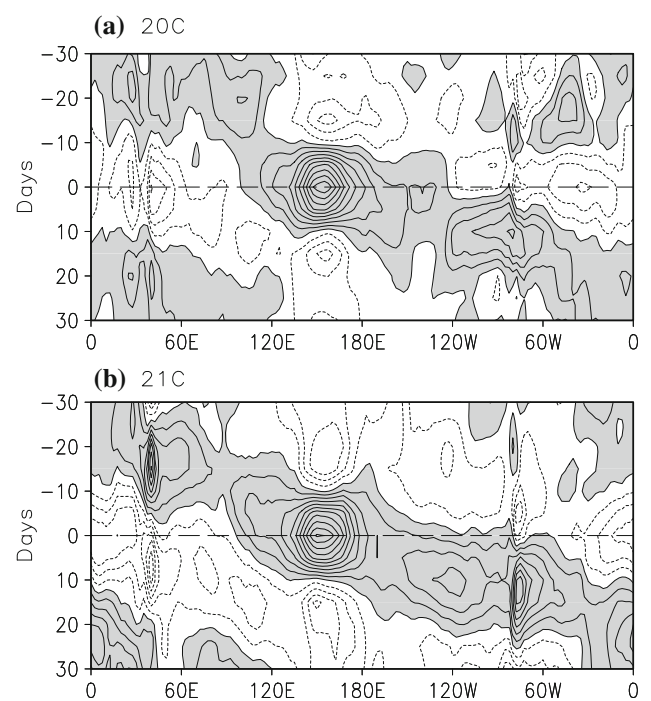


Fig. 9 Same as Fig. 8 but for 850-hPa zonal wind and the reference point is at (155°E, 0°N)

map of the 850-hPa zonal wind. In HIS_20C (Fig. 9a), the eastward propagation circulates the globe with a zonal wavenumber-1 structure. Connections are about 0.1 between the Indian Ocean at about 100°E and at the central Pacific (160°W). In the A1B_21C the connections are strengthened, indicating the warming makes the MJO eastward propagation more prominent.

3.3 Change in composite life cycle of MJO and prominent events

In order to illustrate the change of MJO structure, the number of prominent MJO events, and associated processes with the A1B global warming, we apply an EOF analysis to the 20–100-days band-pass filtered 850-hPa zonal wind after being averaged in 10°S–10°N during the 21 years (1,533 pentads) for the HIS_20C, A1B_21C, and the NCEP-NCAR Reanalysis. This method has been widely used in disclosing the structure and associated mechanisms of a composite MJO life cycle (e.g. Maloney and Hartmann 1998; Liu et al. 2005; Liu 2012). Notably the derived leading EOFs can depict the dominant structure of the MJOs and the corresponding principal components can be used to form an MJO index to select prominent MJO events for analysis and comparison.

Table 1 lists the percentage of the explained to total variance for the leading three EOFs in the three cases. In the NCEP-NCAR Reanalysis the 1st and 2nd EOFs explain 36 and 24 % of the total variance, respectively, while the 3rd EOF accounts for only 8.3 %. The first two EOFs thus contribute predominantly to the MJO structure shown below and both are statistically separable from the rest EOF components using the method of North et al. (1982). In the HIS_20C case the 1st and 2nd EOFs account for 23 and 15.2 % of the total variance, respectively; both are much smaller than those in the NCEP-NCAR Reanalysis. More notably, the 3rd EOF explains 9.6 % of the total variance, making the first two EOFs marginally separable from the rest EOF components. This indicates that the MJO in the HIS_20C is not as prominent as in the observations, which agrees with the power spectral analysis (c.f. Figs. 6, 7). The A1B_21C increases the explained percentage of the total variance to 21 and 19 % for the first two EOFs. However, this increase is marginal and also occurs in the

3rd EOF, suggesting that the A1B global warming strengthens the variance of both the background and MJO-like signals, and it still does not make the MJO significantly separable from the background.

Although the two leading EOFs in the HIS_20C and A1B_21C explain the total variance less significantly than those in the Reanalysis, their spatial structures agree well with those in observations, as shown in Fig. 10. Specifically the observational components have a ridge at 90°E for the EOF1 (solid black) and at 135°E for the EOF2 (solid gray), and a trough near the date line for the EOF1 (solid black) and near 120°W for the EOF2 (solid gray). This wave number one structure is typical for an MJO and is also consistent with the lead-lag correlation maps (c.f. Fig. 8). The structure of the first two EFOs in both the HIS_20C (long dashed) and A1B_21C (dotted) nearly coincides with the typical MJO structure in the Reanalysis. Such a similar structure of the A1B_21C indicates that the warming changes the MJO structure not so much as the magnitude. The similarity enables us to use the first two principal components to form an MJO index so as to disclose the changes in the number of prominent MJO events and the composite life cycles of those events.

The MJO index is defined as $IND(t) = PCI(t) + [PC2(t+2) + PC2(t+3)]/2$, where t denotes time in pentads. The $t+2$ and $t+3$ indicate that the two PCs have largest lead or lag correlation by 2 and 3 pentads although the correlation coefficients for the HIS_20C and A1B_21C are smaller than those for the Reanalysis (not shown). The MJO index time series is then used to identify prominent MJO events. Such an event must consecutively have an initiation (phase 1), a peak (phase 5) and a decay phase (phase 9) that are beyond ± 1 STD of the index value; phases 3 (between 1 and 5) and 7 (between 5 and 9) are close to zero on the index time series, while the rest (2, 4, 6, or 8) correspond to index values falling between phases with consecutive odd numbers. Figure 11 shows the distribution of the selected events for the HIS_20C and

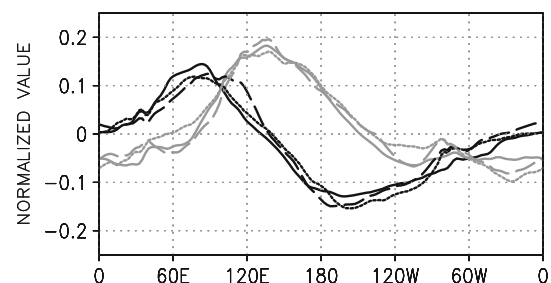


Fig. 10 The leading two EOFs of the 20–100-days band-pass filtered 850-hPa zonal wind along the equator (10°S–10°N mean) during the 21 years (1,533 pentads). *Black* is for the EOF1 and *gray* for the EOF2. *Solid lines* are for the NCEP-NCAR Reanalysis, *long-dashed* for the HIS_20C, and *dotted* for the A1B_21C, respectively

Table 1 Percentage of explained to total variance for the first three EOFs

	EOF1	EOF2	EOF3
NCEP	36	24	8.3
HIS_20C	23	15.2	9.6
A1B_21C	21	19	11

A1B_21C, where the plus signs denote their nine phases. The corresponding index values are in the vertical axis, and the dashed lines represent ± 1 STD. The STD is 14.4 for the NCEP/GPCP, 9.5 for the HIS_20C, and 10.1 for the A1B_21C. The thin black line connects the phases for the composite MJO event that has a period of about 45 days. Clearly with more plus signs, the A1B_21C produces much more prominent MJO events than the HIS_20C does in nearly every phase. The number of complete MJO events is 21 in the NCEP/GPCP, 13 in the HIS_20C, and 27 in the A1B_21C, respectively. The average event in the A1B_21C (thin-black line in Fig. 11b), however, has a very similar shape to that in the HIS_20C except for slightly larger values at the three phases of 1, 5, and 9. This again suggests that the A1B warming does not change the shape of the composite MJO event but enhances its amplitude to some extent.

The number of the peak phase (phase 5) for the selected MJO events is summarized in Fig. 12, where the gray bars represent those in the HIS_20C and hollow bars for those in the A1B_21C. The month axis represents when the peak phase of an MJO occurs. For both cases the peak phases occur in March more frequently than in other months, agreeing with the known fact that the MJO is most active

during boreal spring season. It is interesting that there is no peak MJO phase occurring in February in the HIS_20C. This void may be more related to the accounting method used in this study than a physical reason, given that the number in January is only 2 and that in March is 4. The A1B_21C increases the number of peak phases in every month from December to April. Particularly in February, the number is increased from 0 to 5; and in March from 4 to 7.

We next discuss the mechanisms associated with the simulated and predicted MJO described above. Among the several existing theories, the frictional moisture convergence mechanism consistently describes the MJO structure and its eastward propagation. In that theory (e.g. Wang 1988; Maloney and Hartmann 1998; Sperber 2003; Kiladis et al. 2005; Zhang 2005) near-boundary-layer convergence leads the deep convection associated with MJO in eastward propagation. The convergence produces shallow convection to build up moisture and instability fostering deep convection. Once the deep convection sets up, the MJO phase moves eastward. Therefore the quadrature structure between the low-level convergence and the MJO deep convection characterizes this theory, which has been supported extensively by both observational facts and modeling results (e.g. Maloney and Hartmann 2001; Sperber 2003, 2004; Liu et al. 2005).

The frictional moisture convergence mechanism functions in the composite MJO life cycle for the HIS_20C and A1B_21C cases in spite of some difference, as demonstrated by the composite structure during their peak phases (Fig. 13). Here, the 850-hPa winds are in play, because the boundary-layer winds are not archived and the featured quadrature structure shown below is overall clear. In the NCEP/GPCP case (Fig. 13a) the deep convection (red shading) is located near 90°E, while the 850-hPa convergence (contour and vector) is centered at 130°E. Shallower convection occurs in between these two centers, forming

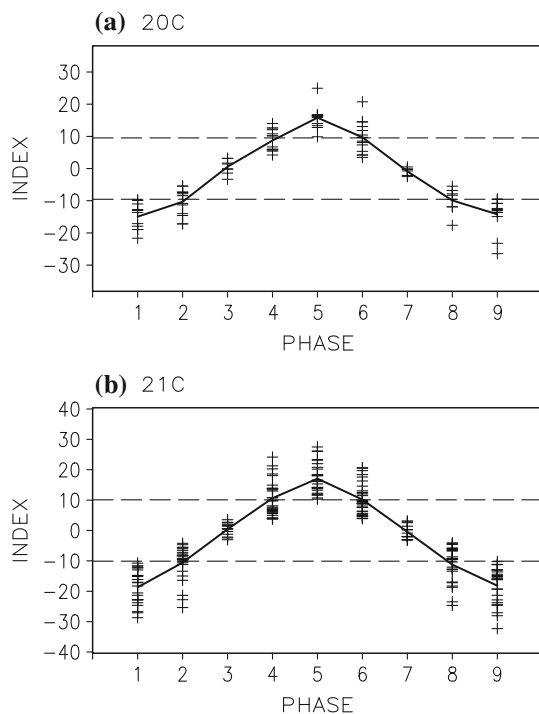


Fig. 11 Phases 1–9 for the composite (solid-black) and for each event in the HIS_20C (a) and the A1B_21C (b), respectively. The dashed lines represent ± 1 STD. The index is defined as $IND = PC1(t) + [PC2(t+2) + PC(t+3)]/2$ where the PCs are the principal components corresponding to Fig. 10. Events that have all phases of 1, 5, 9, and the phase 5 occurs in DJFM season are selected for composite

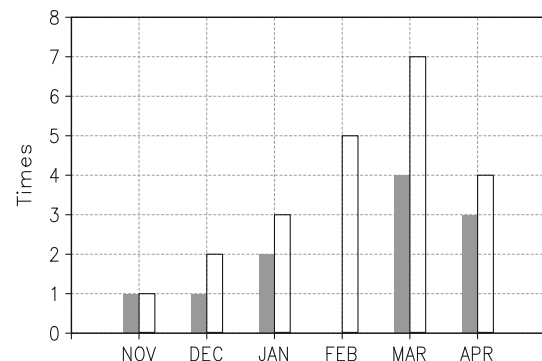


Fig. 12 The number of the peak phases (5) for the events in Fig. 11. Gray bars denote those in the HIS_20C and hollow bars for the A1B_21C

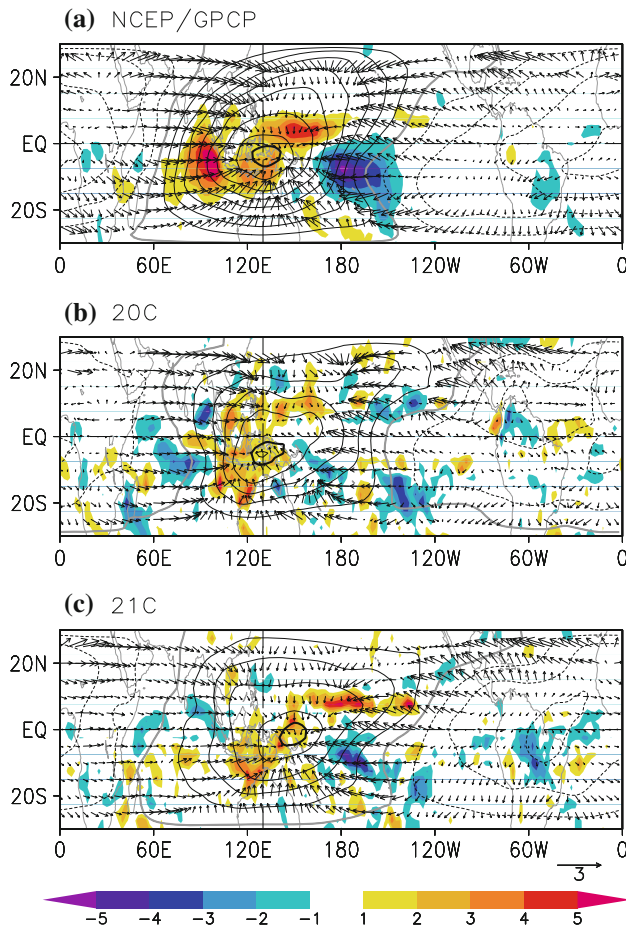


Fig. 13 Composite anomalies of the filtered velocity potential (contour) and divergent wind vector at 850 hPa, and precipitation (color shading, mm day^{-1}) during the phase 5 for **a** the NCEP Reanalysis and GPCP, **b** the HIS_20C, and **c** the A1B_21C, respectively. Solid gray line is for 0, solid-black for **a** 7.6, **b** 4.9, and **c** 4.4, respectively. The thin dashed line represents the 130°E . Contour interval is $1 \times 10^6 \text{ m}^2 \text{ s}^{-2}$

the quadrature structure typical to the MJO. In the HIS_20C case (Fig. 13b) the maximum positive anomalous precipitation occurs near 100°E , and the maximum 850-hPa convergence is located at 130°E . Although the precipitation is weaker and about 10° more east than that in observation, the quadrature structure is clearly produced. In the A1B_21C (Fig. 3c), the precipitation magnitude is slightly larger than that in the HIS_20C, and the center is even closer to the maximum convergence, which makes the frictional moisture convergence less clear.

Another typical structure for the frictional moisture convergence is that the peak precipitation occurs mostly over the 850-hPa westerly wind anomalies (e.g. Sperber 2003; Kiladis et al. 2005). This correspondence is illustrated in Fig. 14 during the composite life cycles for the three cases. In the observations (Fig. 14a), positive anomalous precipitation (red shading) occurs over the 850-hPa

westerly wind anomalies during the nine phases. The magnitude can exceed 2.5 mm day^{-1} for the precipitation anomaly and 0.8 m s^{-1} for the 850-hPa zonal wind. In the HIS_20C (Fig. 14b) case the anomalous precipitation also occurs mostly above low-level westerly anomalies. The magnitude for both anomalous precipitation and 850-hPa zonal wind, however, is smaller than that in observation, which is consistent with the power spectral analysis. The A1B_21C (Fig. 14c) enhances the anomalies to some extent, particularly near 150°E in phase 5. However, the anomalous precipitation occurs more over low-level easterly anomalies, a feature of the non-linear WISHE mechanism (e.g. Maloney and Sobel 2004). Since other variables such as latent heat flux, and wind and specific humidity at the lowest model level are not archived, whether and how much the non-linear WISHE contributes to the MJO and its

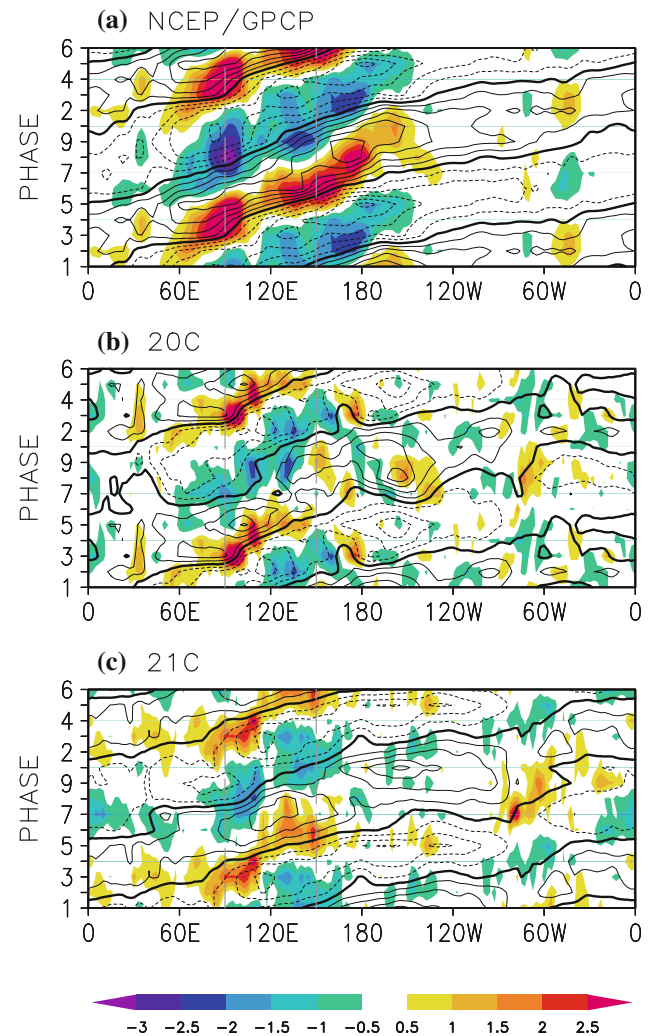


Fig. 14 Anomalies of the filtered 850-hPa zonal wind (contour) and precipitation (color shading) during the 9 phases of the composite MJO. Phases 1–6 are repeated in the upper part of each panel. The contour interval is 0.2 m s^{-1}

possible change merit more study. It is noteworthy that the HIS_20C MJO at upper troposphere is weaker and less coherent with the convection than that in observations, which is also shown in the interannual variation below.

3.4 Interannual variability

The strong interannual variability in the SSTA associated with ENSO does not have a statistically significant relationship with the MJO activities (e.g. Slingo et al. 1999), except for that the MJO signal tends to propagate across the date line farther into the Western Hemisphere during the El Nino years (e.g. Slingo et al. 1999). Here, we show that this loose relationship has been reproduced by the ECHAM5 and it does not change much with the A1B global warming.

The first EOF pattern of SSTA and the corresponding principal component (PC1) based on the 252 months data are shown in Fig. 15 for the HIS_20C and A1B_21C. In the HIS_20C (Fig. 15a) the EOF1 has a typical El Nino pattern, and it accounts for 47.3 % of the total variance. The PC1 reflects three warming and cooling episodes fluctuating irregularly with a life time of 16–24 months. Both the EOF1 and PC1 indicate that a robust ENSO-like signal is produced. In the A1B_21C (Fig. 15b), the SSTA pattern does not change significantly except that the positive center

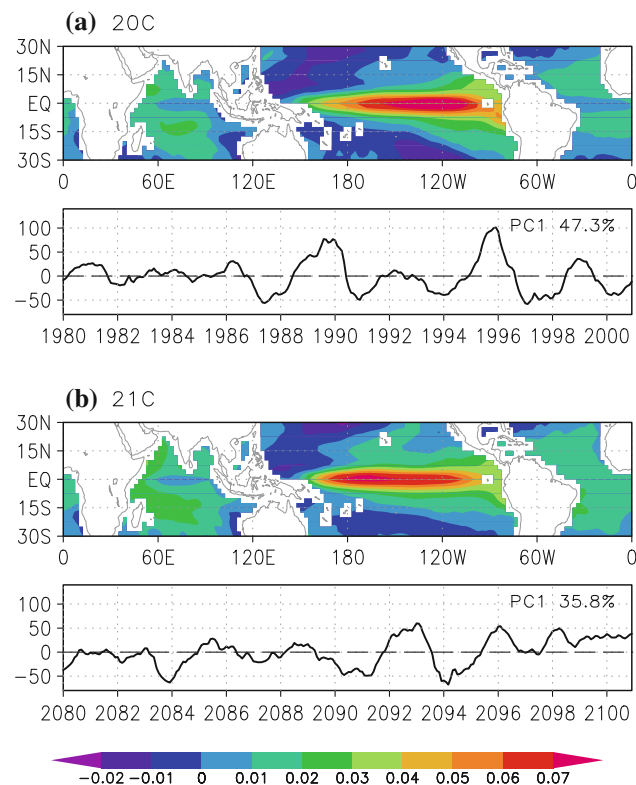


Fig. 15 The 1st EOFs and PCs of the monthly SSTA for **a** the HIS_20C and **b** the A1B_21C, respectively

is shifted somewhat westward along the equator. However, the explained percentage of the total variance drops to 35.8 %, and the maximum amplitude of warm episodes drops to near 50 from about 100 while that of cold episodes changes slightly, suggesting that the A1B warming tends to suppress the El Nino-like signal. Such a change in ENSO can also be depicted by the Nino3 SSTA index shown below.

The interannual variation of MJO can be assessed using the Slingo index (Slingo et al. 1999) but based on 300-hPa zonal wind, which is shown in Fig. 16 for the three cases. In observations during 1979–2000 (Fig. 16a), prominent variations on MJO time scales do not significantly correlate with the ENSO episodes. For example, the Slingo index shows very little MJO activity during the strong El Nino events in 82–83, 87–88, and 97–98; while the MJO is very active in 80–81, 85–86, 87–88, and 96–97 when the SSTA

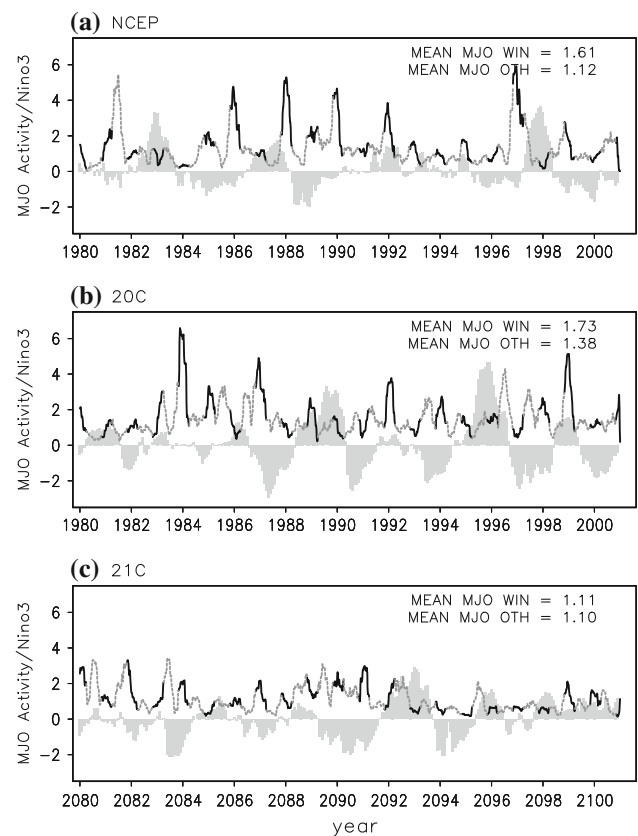


Fig. 16 The MJO (black-gray line) and El Nino activity (gray bar) from **a** the NCEP-NCAR Reanalysis and observation during 1980–2000, **b** the HIS_20C, and **c** the A1B_21C, respectively. The MJO is depicted by the variance ($\text{m}^2 \text{s}^{-2}$) time series of the zonal-mean zonal wind averaged in 10°S – 10°N at 300 hPa. A 20–100-days band-pass filter and a 100-days running mean have been applied to the MJO time series. The black portion represents the MJO events that occurred in the NDJFM season and the gray for the rest. The El Nino is represented by the time series of the monthly mean SSTA ($^\circ\text{K}$) in the Nino3 area (5°N – 5°S , 90°W – 150°W)

depicts weak La Nina episodes. The Slingo index also shows that MJO has a strong seasonality: the averaged index has a value of 1.61 in boreal winter, about 50 % larger than in other seasons when the average index is 1.12. These results are consistent with those reported by Slingo et al. (1999) where shorter records and 200-hPa zonal wind were used. In the HIS_20C (Fig. 16b) the ENSO-like fluctuation is reproduced although the year-to-year events are not, and the amplitude of Nino3 SSTA is comparable to that observed, showing a large variability. Also the MJO has variance comparable to that observed in both magnitude and frequency although there is little event-to-event correspondence: prominent episodes have a Slingo index reaching 6. The MJO also dominates in winter with an averaged index of 1.73 compared to 1.38 in other seasons; both are somewhat higher than those observed, indicating that the model has reasonably reproduced the MJO activity in the upper troposphere during 1980–1999. The interannual variability is clear and not closely related to ENSO (shaded). The A1B warming (Fig. 16c) has suppressed the amplitude of both ENSO and MJO amplitude. This reduced Slingo index indicates that the upper-level MJO is suppressed, which does not agree well with that reported by Slingo et al. (1999). Hypotheses to this disagreement are discussed below.

4 Conclusions and discussions

The ECHAM5/MPI-OM at T63 horizontal resolution projected a 3–4 K warmer tropics under the A1B greenhouse gas emission scenario. Using the derived monthly-evolving SST to force the atmospheric component ECHAM5 at 40-km resolution, simulations of the last 21 years of the twentieth and twenty-first centuries are carried out. Several daily variables archived are employed for the analysis in this study.

Results show that the simulated MJO is still embedded in an over-reddened background, similar to what was reported in the T63 coupled version by Lin et al. (2006). The reproduced MJO has a reasonable EOF structure in low-level zonal winds, but it has much lower-than-observation amplitude and power spectrum in both precipitation and zonal winds. The A1B warming makes the tropics wetter while the variance is enhanced more in background than in other wave bands, suggesting the background becomes even redder. The response of the zonal winds associated with MJO to the enhanced precipitation, interestingly, is different in the lower and upper troposphere. On the one hand based on the 850-hPa zonal wind, the variance is enhanced in the key MJO regions with increased power spectrum while it is suppressed in other areas. The A1B global warming tends to increase the MJO

magnitude, but does not significantly change the structure. The power of changed MJO concentrates on 30–60 days and at zonal wavenumber one in low-level zonal wind rather than scattering in most wavenumbers in precipitation, in spite both changes have passed the 1-tailed Student's *t* test at 90–95 significance percentiles. An MJO index formed by the leading principal components of the 850-hPa zonal winds detects nearly doubled number of prominent MJO events in the A1B_21C than in the HIS_20C. The composite life cycle of these events demonstrates that the frictional moisture convergence mechanism functions to maintain the MJO in the HIS_20C, while the non-linear WISHE also works in the A1B_21C case. These results are mostly consistent with those derived in the aqua-planet experiments by Liu (2012). On the other hand shown by the Slingo index and the Nino-3 SSTA, the A1B warming suppresses the MJO zonal winds in the upper troposphere, and produces the known loose connection between the MJO and ENSO.

The upper-troposphere MJO activity is suppressed by the A1B warming in this model, which contrasts to that reported by Slingo et al. (1999) and can be model dependent. The different MJO change in the lower and upper troposphere can be related to the vertical diabatic heating (e.g. Lin et al. 2004; Lau and Wu 2010), which is presumably enhanced more in the lower than in the upper. Two processes can be further attributed to that change: (1) the shallow convection is enhanced more than the deep convection or even the deep convection is suppressed so that the diabatic heating is strengthened more significantly in the lower troposphere; and (2) the radiative effect of greenhouse gas warming favors low-level amplification. These hypotheses will be investigated using the outputs from the newly available Coupled Model Inter-comparison Project phase five (CMIP5).

In comparison with the coupled version at T63 (c.f. Lin et al. 2006), the high-resolution ECHAM5 does not seem to significantly improve the MJO magnitude, given the over-reddened background in which a weak MJO is embedded. Lin et al. (2006) attributed the arguably best MJO simulation by the T63 coupled version to having convective closure/triggers linked in some way to moisture convergence. The deficiency described in this paper further suggests it be not a resolution issue. This argument can be supported by the yet weak MJO-like signals simulated by a 20-km AGCM (Liu et al. 2009). Possible reasons for the deficiency in the ECHAM5 may be related to the aspects of the revised Tiedtke convection scheme such as the specified strength of convective downdraft, because Liu et al. (2005) reported more realistic MJO and features in a different model using the same scheme but a smaller downdraft. The exact cause probably merits further study.

It has been speculated that the interplay between the convectively coupled waves (CCEWs) was important to the low frequency variability of the tropical atmosphere (e.g. Majda and Biello 2005; Kiladis et al. 2005; Lin et al. 2006). The double ITCZ (Lin 2007) in the HIS_20C and likewise change in the A1B_21C suggest possible contributions of the CCEWs to the modeled MJO. Besides, although the projected MJO is enhanced in magnitude, the change of scale should be cautious because of the overall weak amplitude. The newer coupled models that are participating in the CMIP5 can hopefully provide better simulations and thus projections.

Acknowledgments We thank Dr. Pang-Chi Hsu for helping with the ECHAM5 data. The background power spectrum is derived using the package of Matthew Wheeler and George N. Kiladis. Dr. Andrew Marshall also gave some useful comments. T. Li acknowledged the support by NSF grant AGS-1106536. This study contributes to SOEST (#8742) and IPRC (#911). IPRC is sponsored by JAMSTEC, NASA and NOAA.

References

- Randall DA et al (2007) Climate models and their evaluation. In: Climate change 2007: the physical science basis. Contribution of working group I to the fourth assessment
- Bengtsson L, Hodges KI, Esch M, Keenlyside N, Kornbluh L, Luo JJ, Yamagata T (2007) How may tropical cyclones change in a warmer climate? *Tellus* 59A:539–561
- Hendon HH, Salby ML (1994) The life cycle of the Madden–Julian oscillation. *J Atmos Sci* 51:2225–2237
- Huffman GJ, Adler RF, Arkin P, Chang A, Ferraro R, Gruber A, Janowiak J, McNab A, Rudolf B, Schneider U (1997) The global precipitation climatology project (GPCP) combined precipitation dataset. *Bull Am Meteor Soc* 78:5–20
- Inness PM et al (2003) Simulation of the Madden–Julian oscillation in a coupled general circulation model. Part II: the role of the basic state. *J Clim* 16:365–382
- IPCC (2007) Summary for policymakers. In: Solomon S, Qin D, Manning M, Chen Z, Marquis M, Averyt KB, Tignor M, Miller HL (eds.) Climate Change 2007: the physical science basis. Contribution of working group I to the fourth assessment report of the intergovernmental panel on climate change. Cambridge University Press, Cambridge
- Jones C, Carvalho LMV (2006) Changes in the activity of the Madden–Julian Oscillation during 1958–2004. *J Clim* 19:6353–6370
- Jones C, Carvalho LMV (2011a) Will global warming modify the activity of the Madden–Julian oscillation? *Q J R Meteorol Soc* 137:544–552
- Jones C, Carvalho LMV (2011b) Stochastic simulations of the Madden–Julian oscillation activity. *Clim Dyn* 36:229–246
- Jungclaus H et al (2006) Ocean circulation and tropical variability in the coupled model ECHAM5/MPI-OM. *J Clim* 19:3952–3972
- Kalnay E et al (1996) The NCEP/NCAR 40-year reanalysis project. *Bull Am Meteor Soc* 77:437–470
- Kiladis GN, Straub KH, Haertel PT (2005) Zonal and vertical structure of the Madden–Julian oscillation. *J Atmos Sci* 62:2790–2809
- Lau KM, Wu HT (2010) Characteristics of precipitation, cloud, and latent heating associated with the Madden–Julian oscillation. *J Clim* 23:504–518
- Lin JL (2007) The double-ITCZ problem in IPCC AR4 coupled GCMs: ocean-atmosphere feedback analysis. *J Clim* 20:4497–4525
- Lin JL, Mapes B, Zhang M, Newman M (2004) Stratiform precipitation, vertical heating profiles, and the Madden–Julian oscillation. *J Atmos Sci* 61:296–309
- Lin JL et al (2006) Tropical intraseasonal variability in 14 IPCC AR4 climate models. Part I: convective signals. *J Clim* 19:2665–2690
- Liu P (2012) Changes in a modeled MJO with idealized global warming. *Clim Dyn*. doi:10.1007/s00382-012-1323-2
- Liu P, Wang B, Sperber KR, Li T, Meehl GA (2005) MJO in the NCAR CAM2 with the Tiedtke convective scheme. *J Clim* 18:3007–3020
- Liu P et al (2009) Tropical intraseasonal variability in the MRI-20km60L AGCM. *J Clim* 22:2006–2022
- Madden RA, Julian PR (1971) Detection of a 40–50 day oscillation in the zonal wind in the tropical Pacific. *J Atmos Sci* 28:702–708
- Madden RA, Julian PR (1972) Description of global-scale circulation cells in the tropics with a 40–50 day period. *J Atmos Sci* 29:1109–1123
- Majda AJ, Biello JA (2005) A new multiscale model for the Madden–Julian oscillation. *J Atmos Sci* 62:1694–1721
- Maloney ED, Hartmann DL (1998) Frictional moisture convergence in a composite life cycle of the Madden–Julian oscillation. *J Clim* 11:2387–2403
- Maloney ED, Hartmann DL (2001) The sensitivity of intraseasonal variability in the NCAR CCM3 to changes in convective parameterization. *J Clim* 14:2015–2034
- Maloney ED, Sobel AH (2004) Surface fluxes and ocean coupling in the tropical intraseasonal oscillation. *J Clim* 17:4368–4386
- Nakicenovic N et al (2000) IPCC special report on emissions scenarios. Cambridge University Press, Cambridge
- Nordeng TE (1994) Extended versions of the convective parameterization scheme at ECMWF and their impact on the mean and transient activity of the model in the tropics. ECMWF Tech Memo 206:41
- North GR, Bell TL, Cahalan RF, Moeng FJ (1982) Sampling errors in the estimation of empirical orthogonal functions. *Mon Weather Rev* 110:699–706
- Pham M, Boucher O, Hauglustaine D (2005) Changes in atmospheric sulfur burdens and concentrations and resulting radiative forcings under IPCC SRES emission scenarios for 1990–2100. *J Geophys Res* 110:D06112. doi:10.1029/2004JD005125
- Rayner NA et al (2006) Improved analyses of changes and uncertainties in sea surface temperature measured in situ since the mid-nineteenth century: the HadSST2 data set. *J Clim* 19:446–469
- Roeckner ER et al (2006) Sensitivity of simulated climate to horizontal and vertical resolution in the ECHAM5 atmosphere model. *J Clim* 19:3771–3791
- Slingo JM et al (1996) Intraseasonal oscillations in 15 atmospheric general circulation models: results from an AMIP diagnostic subproject. *Clim Dyn* 12:325–357
- Slingo JM, Powell DP, Sperber KR, Nortley F (1999) On the predictability of the interannual behaviour of the Madden–Julian oscillation and its relationship with El Niño. *Q J R Meteorol Soc* 125:583–609
- Sperber KR (2003) Propagation and the vertical structure of the Madden–Julian oscillation. *Mon Weather Rev* 131:3018–3037
- Sperber KR (2004) Madden–Julian variability in NCAR CAM2.0 and CCSM2.0. *Clim Dyn* 23:259–278
- Tiedtke M (1989) A comprehensive mass flux scheme for cumulus parameterization in large-scale models. *Mon Weather Rev* 117:1779–1800
- Vecchi GA, Soden BJ (2007) Global warming and the weakening of the tropical circulation. *J Clim* 20:4316–4340

- Waliser DE (2006) Intraseasonal variations. In: Wang B (ed) *The Asian monsoon*. Springer, Heidelberg, p 787
- Waliser DE et al (1999) A statistical extended-range tropical forecast model based on the slow evolution of the Madden–Julian oscillation. *J Clim* 12:1918–1939
- Wang B (1988) Dynamics of tropical low-frequency waves: an analysis of the moist Kelvin wave. *J Atmos Sci* 45:2051–2065
- Wang B, Rui H (1990) Dynamics of the coupled moist Kelvin–Rossby wave on an equatorial β -plane. *J Atmos Sci* 47:397–413
- Wheeler M, Hendon HH (2004) An all-season real-time multivariate MJO index: development of an index for monitoring and prediction. *Monthly Weather Rev* 132:1917–1932
- Wheeler M, Kiladis GN (1999) Convectively coupled equatorial waves: analysis of clouds and temperature in the wavenumber-frequency domain. *J Atmos Sci* 56:374–399
- Yasunari T (1979) Cloudiness fluctuation associated with the Northern Hemisphere summer monsoon. *J Meteorol Soc Jpn* 57:227–242
- Zhang C (2005) Madden–Julian oscillation. *Rev Geophys* 43:RG2003. doi:[10.1029/2004RG000158](https://doi.org/10.1029/2004RG000158)
- Zhang M, Song H (2006) Evidence of deceleration of atmospheric vertical overturning circulation over the tropical Pacific. *Geophys Res Lett* 33:L12701. doi:[10.1029/2006GL025942](https://doi.org/10.1029/2006GL025942)